Materials & Design 216 (2022) 110572

Contents lists available at ScienceDirect

Materials & Design

journal homepage: www.elsevier.com/locate/matdes

Cellulose nanocrystals to modulate the self-assembly of graphene oxide in suspension

Vikram Singh Raghuwanshi [a,1,*], Swambabu Varanasi [b,1], Warren Batchelor [a], Gil Garnier [a,*]

[a] Bioresource Processing Research Institute of Australia (BioPRIA), Department of Chemical Engineering, Monash University, Clayton, Victoria 3800, Australia

[b] Department of Chemical Engineering, Indian Institute of Technology-Kharagpur, Kharagpur, West Bengal, India

HIGHLIGHTS

- The self-assembly of graphene oxide (GO) sheets and cellulose nanocrystals rods (CNC) in CNC/GO composite suspension is studied by SAXS.
- Mixing isotropic and nematic phases of CNC with GO at different CNC/GO ratios shows transition from isotropic to biphasic and a nematic state.
- At a higher CNC/GO ratio, the CNC rods force the GO sheets to align in the direction of the CNC nematic assembly.
- This novel self-assembly mechanism of CNC-GO composites can prevent graphene aggregation on reduction for specific application.

GRAPHICAL ABSTRACT

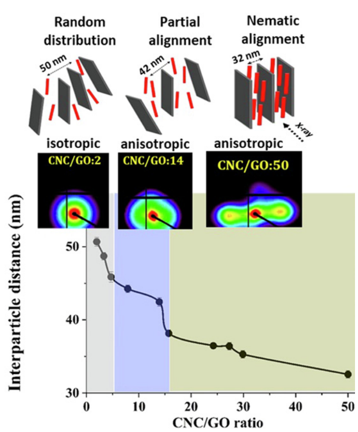

ARTICLE INFO

Article history:
Received 9 November 2021
Revised 17 March 2022
Accepted 18 March 2022
Available online 22 March 2022

Keywords:
Cellulose nanocrystals
Graphene oxide
Self-assembly
Isotropic
Nematic
Small angle X-ray scattering

ABSTRACT

Controlling the self-assembly(SA) of cellulose nanocrystals(CNC) and graphene-oxide(GO) sheets at nanoscale is crucial for exploiting properties of both CNC and GO. The SA mechanism of GO, CNC and CNC/GO in suspension is evaluated at different concentrations and mixing ratios. SAXS determine the interparticle distance, interaction and distribution of CNC and GO to resolve the self-assembling mechanism. At lower concentrations, the GO sheets are distributed randomly and separated by a large inter-sheet distance of 83 nm with poor inter-sheet interaction. As increases the GO concentration, the inter-sheet repulsion results in a nematic arrangement with the inter-sheet distance decreasing from 83 to 52 nm. Mixing isotropic and nematic phase of CNC with GO at different CNC/GO ratio from 2 to 50 shows transitions from isotropic, to biphasic and nematic state. In isotropic state, at low CNC/GO ratio, the GO sheets are randomly distributed between the CNC rods which increases the CNC inter-rod distance from 22 to 51 nm. However, at higher CNC/GO ratios, steric repulsion from the large amount of CNC forces the GO sheets to align following the direction of CNC nematic assembly. Understanding SA mechanisms of nanostructures in CNC-GO hybrid will enable to engineer applications for sensor, electronics and diagnostics.

* Corresponding authors at: Bioresource Processing Research Institute of Australia (BioPRIA), Monash University, Clayton, Vic-3800, Australia
E-mail addresses: Vikram.raghuwanshi@monash.edu (V. Singh Raghuwanshi), gil.garnier@monash.edu (G. Garnier).

[1] Vikram Singh Raghuwanshi and Swambabu Varanasi are both first authors and equally contributed.

https://doi.org/10.1016/j.matdes.2022.110572
0264-1275/© 2022 The Authors. Published by Elsevier Ltd.

1. Introduction

In the recent years, graphene has received a strong and growing interest for its superior electronic [1,2], thermal [1,2], and mechanical properties [3]. It is being used in various applications of optoelectronics [4], energy-storage [3], and sensors [5,6]. Graphene consists of several single layers of hexatomic ring of carbon atoms and is prepared by mechanical or chemical exfoliation and chemical vapour deposition. Of these techniques, chemical reduction of graphene oxide (GO) is one of the most efficient and inexpensive process to prepare graphene in large quantities [7]. However, during the reduction of graphene oxide (GO), the individual graphene sheets tend to stack and bound by $\pi - \pi$ interactions [8] and weak van der Waals forces [9]. Thus, it is required to find processes to inhibit graphene sheets stacking during this critical GO reduction.

To promote the widespread application of graphene and to produce graphene-based macro materials, the integration of individual graphene nanosheets into ordered macroscopic materials is crucial [10,11]. Many types of materials were intercalated between the GO layers followed by reduction to prevent stacking of graphene nanosheets or prepare stable graphene-based macro materials [12]. This technique leads to graphene hybrids materials in form of fibres [13], hydrogels [14], foams and films [15]. Among those, carbon nanotubes (CNT) were used as intercalated layers of GO and CNT's producing hybrid materials as free-standing fibres and papers sheets [16–18]. Cellulosic nanomaterials, such as cellulose nanocrystals (CNC) and cellulose nanofibers (CNF), were investigated as spacer between graphene layers or nanosheets to effectively reduce π-π stacking interactions [19,20]. Hybrid graphene materials prepared with cellulosic nanomaterials demonstrated superior performance compared to the graphene alone [19,20].

Graphene oxide has useful functionalities such as hydrophilicity, high surface activity and antifouling properties attributable to its oxygen-containing groups including epoxy, hydroxyl and carboxyl. However, pristine GO membranes suffer from low permeation flux and weak structural stability in the wet state. The addition of CNC to GO enhances the mechanical strength of the membranes and its permeation flux [21,22]. The controlled self-assembly of CNC/GO in a composite induces the advantageous properties of both CNC and GO. Both CNC and GO display liquid crystal self-assembly ability in suspension once a threshold concentration has been reached; this makes CNC-GO hybrids attractive for optical and electronics applications. The chemical reduction of CNC/GO hybrid produces electrically conductive filaments with good mechanical properties [10]. The CNC/GO hybrids can be engineered into filaments, thin films, membranes, fibres, foam and gel form. These hybrids of improved properties are used in different types of functional materials: biohybrid aerogels, smart composites [47], energy storage as supercapacitor [10,23], water purification [24], sensors [25] emulsions, and membranes [26]. The functionality and properties of CNC/GO hybrids strongly depends on the CNC and GO nanosheets interactions and the resultant self-assembly network formation by intra- and intermolecular hydrogen bonds. The mechanisms of self-assembly and the type of interaction between CNC nanorods and GO sheets in the hybrids are poorly understood; this is in good part due to the lack of specific structural characterization required to elucidate those.

This study aimed to determine the interparticle distance, the interaction and distribution of CNC and GO in the suspension to resolve the self-assembling mechanism. CNC/GO hybrids were prepared by mixing their constitutive suspensions at different CNC/GO ratio ranging from 2 to 50. Small angle X-ray scattering (SAXS) was selected to characterize the suspensions and evaluate the CNC-GO self-assembly mechanism using the high X-ray flux of the Australian synchrotron. Isotropic and anisotropic scattering is used to characterize the orientational assembly of CNC and GO at different concentrations and ratios. In addition, the averaged SAXS curves are used to evaluate the morphology, changes in the interparticle distance, and interaction between CNC and GO in the hybrid suspension. With increase in the CNC/GO ratio, a phase diagram showing the transition from isotropic to nematic arrangements is plotted. This new knowledge gained in this study can help to further expand the applications of CNC/GO hybrids in electronics, photonic materials and optical devices.

2. Experiments

2.1. Materials

Cellulose nanocrystal (CNC) suspension of 12.6 wt% concentration was purchased from the University of Maine Process Development Centre, USA. The available information of the CNC from the vendor are: Fiber dimensions: 5–20 nm wide 150–200 nm long, sulfur content of 1.1 wt%, density: 1.0 g/cm^3 aqueous gel. The CNC was diluted in MilliQ water as needed. Milli-Q water has the conductivity of 0.055 microsiemens/cm. Graphene oxide (GO) sheets were provided by Prof. Mainak Majumder, Monash University, Australia. GO preparation details were given in [27]. For the SAXS measurements 1 mm thick quartz capillaries were bought from the Charles Supper Company, Massachusetts 01,581 USA.

2.2. CNC-GO suspension

Never-dried 12.6 wt% CNC suspension and 1 wt% GO suspension were diluted to various concentrations by adding the required amount of water, followed by sonication. To produce suspensions with various CNC/GO ratios, 12.6 wt% CNC suspension and 0.9 wt % GO suspension were mixed at the required ratio. The total volume of suspension increased when the CNC/GO ratio increased. For example, to prepare a suspension with a CNC/GO ratio of 24, 3.58 g of GO suspension and 6.13 g of CNC suspension were mixed. For all ratios of CNC/GO, the total volume of suspension was ensured to be lower than 10 mL. A similar precaution was taken while diluting the CNC and GO suspensions. Depending upon its volume, the suspension (either CNC, GO or CNC/ GO) is sonicated in either a 5 mL or 10 mL glass vial. Sonication is performed with a titanium probe (Sonics Vibra-cell High-Intensity Ultrasonic Processor, VCX 500–VCX 750) immersed in the suspension under the following conditions: 3 sec- on and 3 sec- off for an interval of 3 min, with a total energy input of 4750 J regardless of the sample concentration. Ultrasonication was carried out at a minimum energy level of 500 kJ/g.L; it is higher than the optimal energy level of 200 kJ/g.L recommended by Girard et al [46]. For example, for the suspension having a CNC/GO ratio of 24, a total 9.71 g of CNC and GO suspension was sonicated for 3 min with an energy input of 4750 J. Standard sonication energy was estimated to be 633 kJ/g.L. For the SAXS measurements, the CNC, GO, and CNC-GO suspensions were filled in 1 mm thick quartz capillaries. The prepared capillaries were mounted for SAXS measurements within one hour after sonication. The complete SAXS measurements took about 30 min. Precautions were taken to measure quickly, as the rheology of a CNC suspension - changes drastically with time, especially after one day.

2.3. Small angle X-ray scattering (SAXS)

SAXS measurements of the composite liquid suspension were performed at the SAXS/WAXS beamline of the Australian Synchrotron, Australia [28]. SAXS measurements were made at an energy of 12 keV (λ = 1.033 Å) at 2 sample to detector distances (7 m and 1 m) covering the q range between q = 0.001 and 0.2 $Å^{-1}$. The scattered X-rays from the sample were collected using a PILATUS 1 M detector (pixel size 172 μm × 172 μm). Silver behenate was used to calibrate the q scale. Scattering curves were normalized to an absolute scattering cross section by the pre-calibrated scattering curve of the glassy carbon. Final scattering curves were extracted after the data reduction and radial averaging was done using the beamline specific ScatterBrain software.

2.4. Atomic force microscopy (AFM)

Atomic force microscopy (AFM, JPK Nanowizard 3) was used in alternating contact, AC mode to obtain images of CNC morphology and particle size. CNC suspension drop was casted, and air died on glass slide.

3. Results

Individual and combined aqueous suspensions of cellulose nanocrystals (CNC) and graphene oxide (GO) were prepared at different concentrations and compositions. Both CNC and GO show isotropic to nematic structural arrangements depending on their concentration in the aqueous suspension [26]. Small angle X-ray scattering (SAXS) experiments were performed to determine the self-assembly and interactions of GO and CNC in the hybrid suspensions. SAXS is a powerful non-destructive analytic method capable of determining the nanostructures' shape, size, distribution, interactions, as well as providing information on the assembly mechanisms at the 1–100 nm length scale [29–32]. The 2D SAXS detector images of the GO aqueous suspensions at GO concentrations of 0.2 wt%, 0.7 wt% and 1.0 wt% are shown in the Fig. 1A. The lower GO concentration (0.2 wt%) sample shows isotropic scattering indicating random distribution of GO sheets in the suspension. Increasing GO concentration to 1.0 wt% results in an anisotropic scattering, revealing the GO sheets to be arranged and oriented in a particular direction.

Further description of the GO sheets self-assembly was achieved by radial averaging of the SAXS images (Fig. 1B). The SAXS curve intensity is plotted as a function of scattering vector q ($Å^{-1}$). The scattering vector q is related to the scattering angle θ and the incident X-ray wavelength (λ) by:

$$q = 4\pi \sin(\theta)/\lambda \tag{1}$$

The SAXS curve for the GO lower concentrations (0.1 wt% and 0.2 wt%) follows the power-law $I(q) = cq^{-\alpha}$ slope at the lower q values ($q < 0.005$ $Å^{-1}$) without any evidence of correlation peak. The slope value of α = 2 reveals the scattering originates from a randomly oriented GO sheet.

The SAXS curve for the higher concentration of GO (0.6 wt%) shows a correlation peak at q = 0.0075 $Å^{-1}$, indicating the self-assembly of GO sheets in a nematic order [33]. With the further increase in GO concentration, the correlation peak becomes sharper and moves towards higher q values. For the suspension at the highest GO concentration of 1.0 wt%, the correlation peak shifts to the higher value of q = 0.012 $Å^{-1}$. The clarity in the correlation peak is visualised in the Kratky plot of the SAXS curves ($I.q^2$ vs q) (Fig. 1C). Higher scattering intensity indicates an increase in the volume fraction as increases the GO concentration. The sharpness

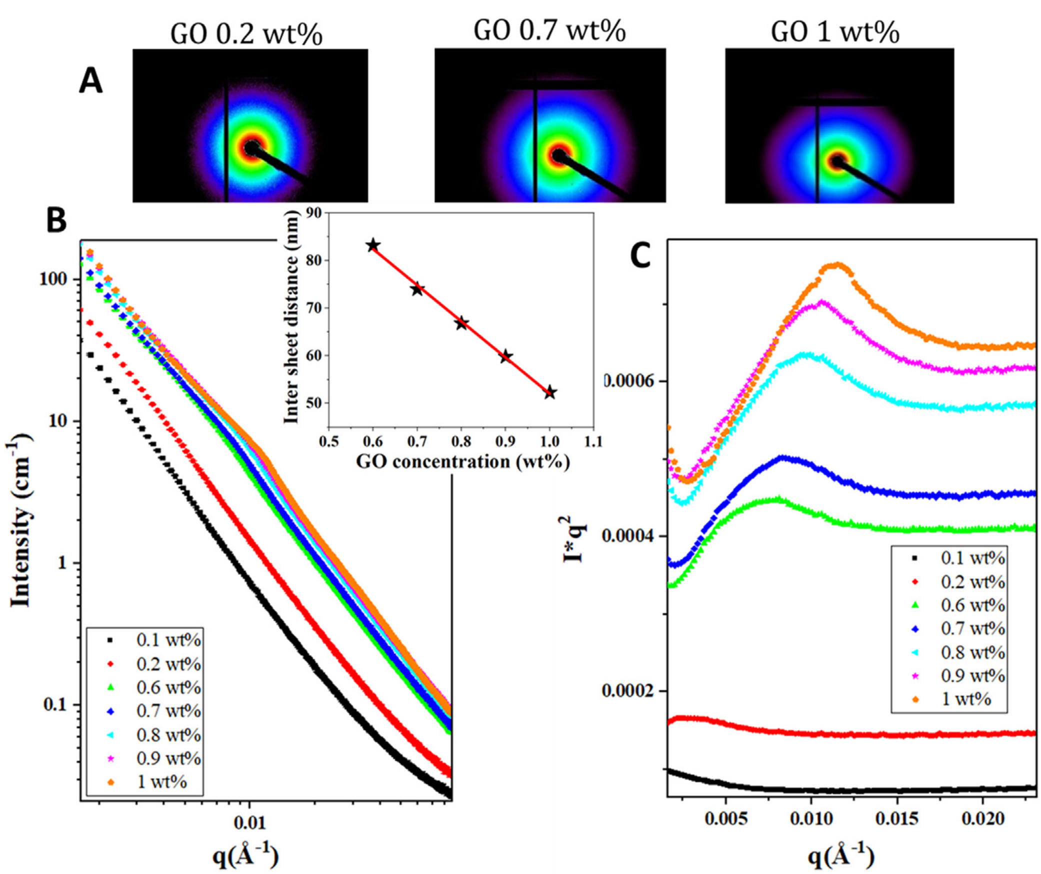

Fig. 1. (A) SAXS scattering images of showing the different phases of graphene oxide (GO) suspensions at concentrations of 0.2 wt% (isotropic), 0.7 wt% (isotropic) and 1 wt% (anisotropic). (B) Radial averaged SAXS intensity-q curves for GO suspensions at different concentrations ranging from 0.1 wt% up to 1 wt%. GO concentration versus inter sheet distance in nanometres (inset). (C) Kratky plot of the SAXS curves.

of the peak reveals a better ordering or self-assembly of the GO sheets.

The shift of q value towards higher values indicates a decrease in the interplanar (sheets) distance. The interplanar distance between GO sheets is evaluated from the correlation peak position q^* by the relation:

$$d = 2\pi/q^* \tag{2}$$

where 'd' is the inter sheet distance. The evaluated 'd' value for the GO concentration of 0.6 wt% is 83 ± 2 nm, decreasing to 52 ± 1 nm upon increasing the GO concentration to 1 wt%. The plot of inter sheet distance as a function of GO concentration between 0.6 and 1 wt% shows a linear relationship (Fig. 2B inset). The results indicate that with an increase in GO concentration, the GO sheets come close to each other in ordered nematic self-assembly.

Structure morphology and self-assembly of CNC rods in the suspension is studied by SAXS and atomic force microscopy (AFM) of the suspension air dried on a glass surface. The SAXS image of the CNC 12 wt% suspension shows partially anisotropic scattering due to the chiral nematic structure (inset Fig. 2A). The radial averaged SAXS curve shows a strong correlation peak at q^*= 0.028 $Å^{-1}$ which reveals an interrod distance of 23 ± 2 nm (Fig. 2A). A CNC suspension at a lower concentration of 3 wt% shows a weak correlation peak at the lower q value of q^*=0.008 $Å^{-1}$, as shown in the SAXS Kratky plot comparison in Fig. 2B. The correlation peak corresponds to a larger inter rod distance of 70 ± 2 nm. The SAXS curve fits well with a long cylinder model (rod) of length 150 ± 5 nm and diameter of 6 ± 2 nm. The rod radius distribution is shown in the inset of the Fig. 2B which reveals an average diameter of 6 nm. The AFM visualise the rod like morphology of the CNC with thickness ranges up to 10 nm (Fig. 2C). The parameters obtained from the AFM are in consistent with the SAXS data analysis.

The CNC-GO hybrid suspensions were prepared by mixing CNC rods and GO sheets at different CNC/GO ratios ranging from 2 to 50. The SAXS experiments show isotropic scattering for the CNC/GO ratio of 2 to 5 (Fig. 3A). Increasing the CNC/GO ratio up to 14 shows transformation from isotropic to partially anisotropic scattering (Fig. 3A). Fig. 3B shows SAXS curves obtained after radial averaging of the scattering images. A correlation peak is observed in all SAXS curves, which shifts towards higher q values with an increase in CNC/GO ratio from 2 to 14. The clarity in the correlation peak is seen in the Kratky plot (inset Fig. 3B). The interparticle distance evaluated from the correlation peak at the lower CNC/GO ratio 2 is 50.7 ± 0.6 nm, which reduce to 42.5 ± 0.6 nm at the higher CNC/GO ratio of 14. The scattering intensity increases with an increase in the CNC/GO ratio, which indicates an augmentation in the volume fraction in the suspension. The sharpness of the correlation peak also increases, revealing more CNC rods with the GO sheets are arranging in a nematic order structure.

Further information from the scattering curves is extracted by fitting them with a form factor combined with a distribution function. The GO/CNC SAXS curves fit well with a combination of a sheet and a long cylinder form factor with log-normal distribution function. A structure factor is included in determining the interparticle interactions between CNC rods. The best fitting parameters show a GO sheet thickness of 1 nm, and a CNC cylinder of 6 nm in diameter, and a length of 150 nm. The structure factor for suspensions of different CNC/GO concentrations is shown in Fig. 3C. The structure factor peak becomes sharper and shifts towards higher q values as increases the CNC/GO ratio. Sharpness in the structure factor peak indicates an increase in the interrod interaction while the shift of peak towards a higher q value reveals a decrease in the interrod distance [31,34,35].

Further increase in the CNC/GO ratio from 16 to 50 reveals a transition from semi-isotropic to the nematic phase. Fig. 4A shows the 2D SAXS scattering images for the CNC/GO at three higher ratios of 16, 24 and 50, which shows anisotropic scattering. The anisotropy in the scattering reveals the orientation of the CNC and GO nanostructures in an ordered assembly. Radial averaging of scattering images allows choosing only lower q values for the

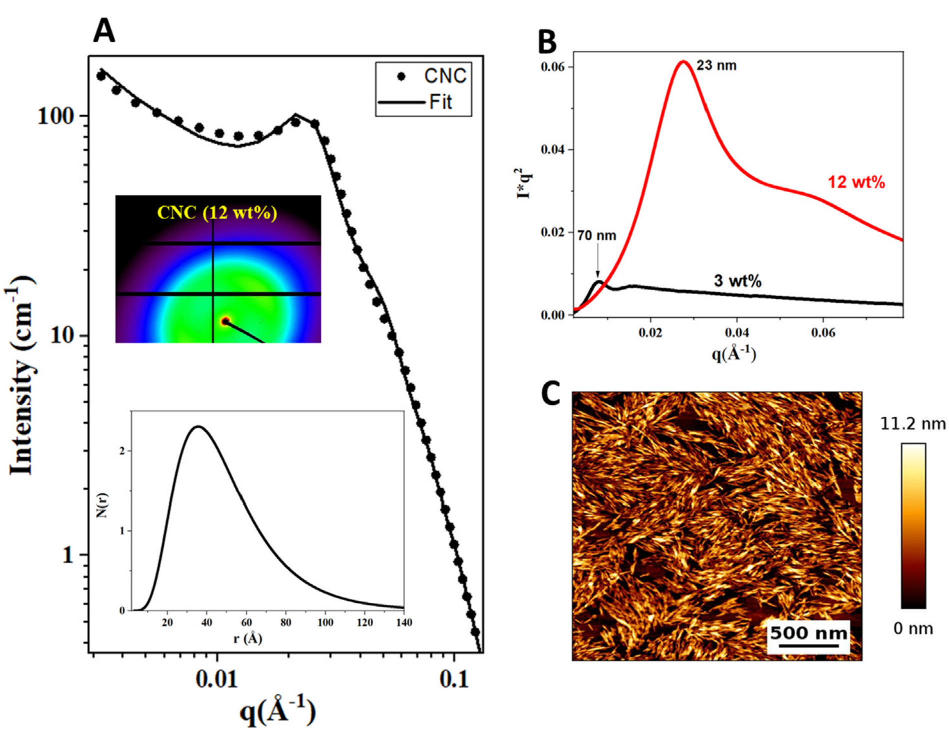

Fig. 2. (A) Radial averaged SAXS curves for the 12 wt% cellulose nanocrystal (CNC) suspension. SAXS scattering image of the 12 wt% CNC (inset). Radius distribution of the CNC rod evaluated by SAXS curve fitting of the CNC 12 wt% suspension(inset). (B) Kratky plot comparison for SAXS curve of 12 wt% and 3 wt% CNC suspensions. (C) AFM of the pure CNC (12 wt%) dried on glass surface with the height profile ranges up to 10 nm.

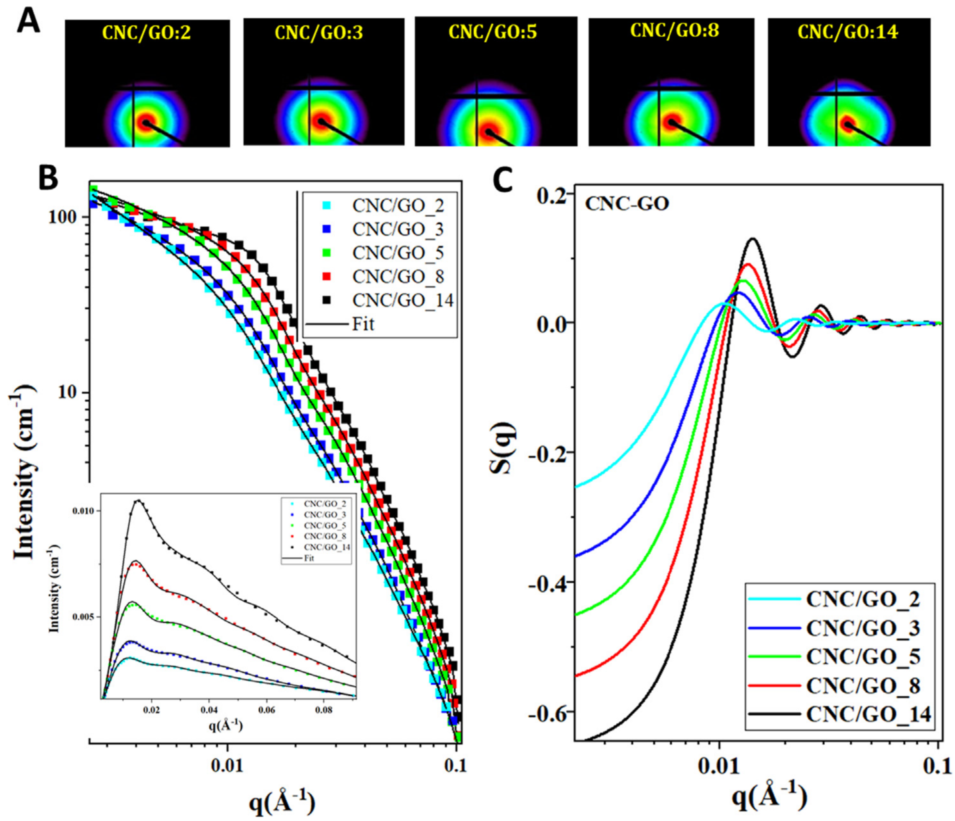

Fig. 3. (A) SAXS scattering images for the CNC-GO suspensions prepared at different ratios: 2, 3, 5, 8 and 14. (B) Radially averaged SAXS curves of the scattering images. Kratky plot of the SAXS curves (inset). (C) Resulting structure factor evaluated by SAXS curve fitting.

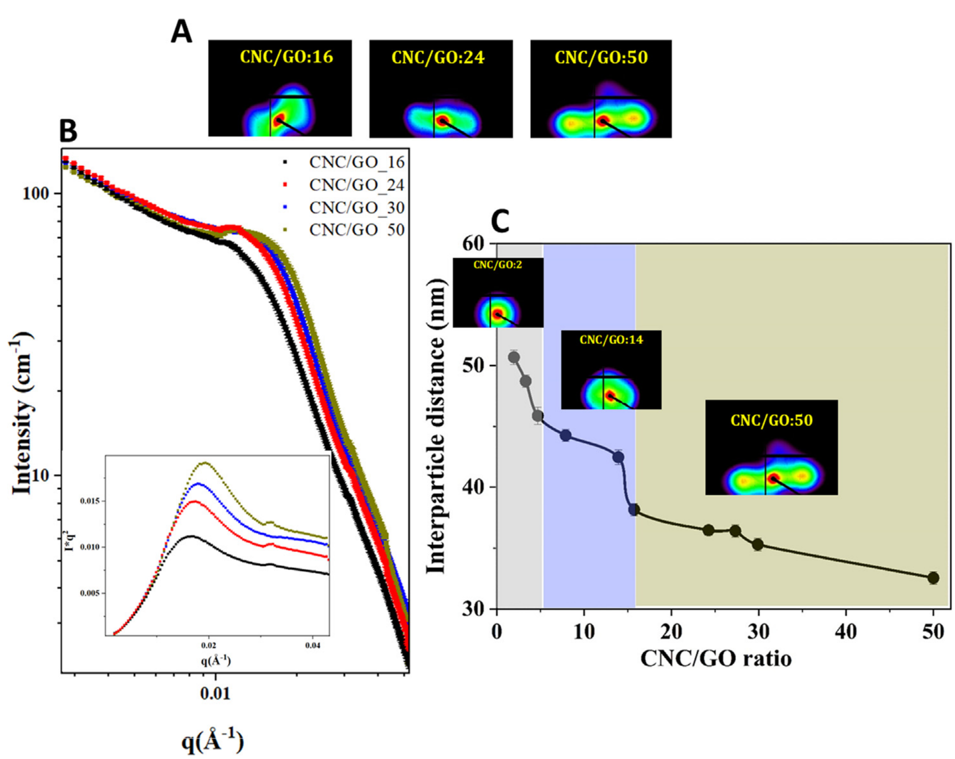

Fig. 4. (A) SAXS scattering images for the CNC-GO suspensions prepared at different ratio of: 16, 24, 30, and 50. The concentrations are provided in the supporting information S1. (B) Radially averaged SAXS curves of the scattering images. Kratky plot of the SAXS curves (inset). (C) Plot of inter particle distance as a function of CNC/GO ratio from 2 to 50 mapping the isotropic, biphasic and nematic ordered states, respectively.

analysis, due to anisotropy in the scattering. All SAXS curves in Fig. 4B show a correlation peak which is clearly seen in the Kratky plot (inset Fig. 4B). The correlation peak reveals the interrod distance (d) of 38.2 ± 0.5 nm for the CNC/GO ratio of 16, which reduce to 32.5 ± 0.5 nm at the highest CNC/GO ratio of 50.

A plot of the interrod distance as a function of the CNC/GO ratio from 2 to 50 is shown in Fig. 4C. A table is provided in the supporting information highlighting CNC and GO concentration, CNC/GO ratio and calculated interparticle distance (S1). Three different regions are observed with two transition boundary lines: Region (I) - between CNC/GO ratio 2 to 5, Region (II) -between CNC/GO ratio of 5 and 15 and Region (III) -between CNC/GO ratio 16–50. These transition regions indicate changes in the assembly of the CNC rods and GO sheets in isotropic, biphasic and nematic ordered states with respect to different CNC/GO ratios.

4. Discussion

Cellulose nanocrystals (CNC) are rod like crystalline structures obtained from the acid hydrolysis of cellulose fibres. The large amount of sulphate and hydroxyl groups on the CNC surface provides their high zeta potential of −30 mV to −60 mV and thus produces a stable suspension. Depending on the concentration, structure and surface groups, the CNCs self-assemble in different states: isotropic (at low concentration), nematic and chiral nematic at high concentration [36]. The partially isotropic SAXS image of the 12 wt% CNC suspension reveals the formation of a self-assembled chiral nematic structure. SAXS curve fitting reveals the CNC rods are 6 nm in diameter, 150 nm long and the correlation peak at q = 0.028 Å^{-1} shows an interrod distance of 23 ± 2 nm (Fig. 2). Suspension at a lower concentration of CNC (3 wt%) shows isotropic CNC arrangement with large inter-rod distance of 70 ± 2 nm. Similar inter CNC rod distance of 24.5 nm was reported previously for 10 wt% CNC suspensions [37]. Incorporating organic and inorganic nanoparticles or salts affects the interrod distance and varies the CNC self-assembly structure [36,38,39].

Graphene oxide (GO) has a 2D sheet-like morphology of thickness 0.8–1.5 nm and length ranging from 100 nm to a few micrometres [27]. Similar to the CNC, the GO suspension has a negative surface charge and shows a transition from isotropic to nematic self-assembly after a threshold concentration [33]. At a lower GO concentration (up to 0.2 wt%), the GO sheets are distributed isotropic (randomly), which is observed in the isotropic SAXS scattering images (Fig. 1A). In the radially averaged SAXS curves, no correlation peak is observed for 0.1 wt%, while a weak correlation peak at q*=0.002 Å^{-1} is monitored for 0.2 wt%. The correlation peak reveals a large inter sheet distance of 314 ± 5 nm. In the isotropic phase, the GO sheets stay away from each other due to electrostatic repulsion and move freely because of Brownian motion and poor inter sheet interactions (Fig. 5A).

For suspensions at a higher GO concentration (0.6 wt%), a sharp correlation peak in the SAXS curve at q*= 0.0076 Å^{-1} corresponding to the shorter inter-sheet distance of 83 nm is observed. At higher concentrations, the GO sheets come closer together, and due to electrostatic repulsion, the GO sheets align towards a nematic phase. The SAXS scattering image is still isotropic, revealing that the sheets are not perfectly aligned. Thus, this concentration region is a transition biphasic state between isotropic and nematic state. Increasing GO concentration to 1 wt% produces anisotropic SAXS scattering indicating orientation of GO sheets in a direction perpendicular to the incident X-rays direction (Fig. 5B). As the number of sheets per volume increases, the GO sheets come closer and the extensive inter-sheet repulsive force assemble them in a nematic arrangement (Fig. 5B). The inter sheet distance reduces to 52 nm as reflected in the SAXS correlation peak shift to q*=0.012 Å^{-1}.

CNC and GO suspensions are mixed at different CNC/GO ratios ranging from 2 to 50. At a lower ratio of 2 to 5, the isotopic phase of CNC and the nematic phase of GO produce isotropic SAXS scattering confirming the random orientation of CNC and GO. However,

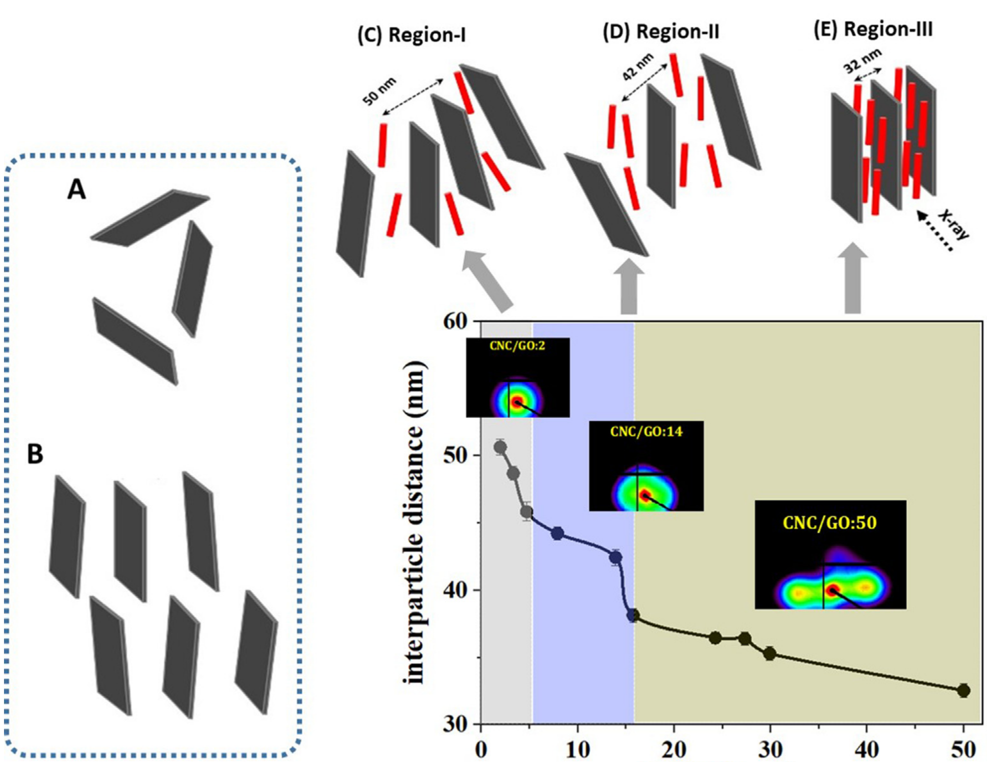

Fig. 5. Schematic of the GO and GO/CNC self-assembly in suspensions of different concentrations. (A) Isotropic arrangement of graphene oxide at the lower concentration. (B) Nematic arrangements of graphene oxide at the higher concentration. (C) Self-assembly at the lower CNC/GO ratio. (D) Self-assembly at the intermediate CNC/GO ratio (E) Self-assembly at higher nematic CNC/GO ratio arranging CNC and GO in nematic phase.

a correlation peak at q = 0.012 $Å^{-1}$ in the SAXS curve (ratio 2) shows the inter CNC rod distance of 50.7 nm (Fig. 3B) which is more than twice that of pure CNC interrod distance (23 nm). In the CNC-GO suspension, the GO sheets penetrate between the CNC rods and by electrostatic repulsion, the GO inhibit the alignment in nematic structures. Thus, GO sheets intercalated between the CNC rods increase the inter-rod distance (Fig. 5C).

Increasing the CNC/GO ratio from 2 to 5, shifts the SAXS correlation peak towards higher q with increase in sharpness confirming an increase in the assembly of nanostructures. Increasing the CNC amount enhances the repulsive forces in the system which constraints the GO sheets to align in the direction of the CNC rod orientation. This brings the CNC rods close to each other as signified by the reduction in the inter-rod distance decreasing from 51 nm to 46 nm. The ratio between 2 and 5 is an isotropic state with a transition towards biphasic state occurs at 5 (Fig. 5D).

Increasing the CNC/GO ratio of the suspension (>5) continues the biphasic state up to a ratio of 14 at which the inter rod distance linearly declines from 46 nm to 38 nm. The partially anisotropic SAXS scattering reveals the CNC and GO are partially oriented in the nematic structure (Fig. 3A). In this region, an increase in the CNC amount further forces the GO sheets to align in the direction parallel to the rod assembly and reduces the inter-rod distance. However, the CNC and GO sheets are still partially aligned (Fig. 5D). A transition occurs at the CNC/GO ratio between 14 and 16 where the inter-rod distance decreases from 42 nm to 38 nm.

Upon increasing the CNC/GO ratio from 16 to 50, the inter-rod distance linearly decreases from 38 to 32 nm. In this region, the SAXS scattering is anisotropic confirming the complete orientation in the nematic state assembly. In this state, the CNC rod overcome the disruptive effect of the GO sheets, and the large amount of CNC rods organises into the nematic phase. The CNC rods exert repulsive force on the GO sheets to align in parallel to the nematic direction of the CNC assembly (Fig. 5E). The phase for suspensions at CNC/GO ratio ranging between 16 and 50 is completely nematic. Similar alignment of gold nanorods along the axis of CNC was reported previously [36]. A plot of interparticle distance as a function of CNC/GO ratio maps the three different regions of isotropic, transition and nematic states. Thus, depending on the CNC/GO ratio the assembly of CNC and GO changes from isotropic to transition to the nematic phase.

The self-assembly of nanostructures at the nanoscale depends on different factors such as nanostructure geometry, surface chemistry, and different covalent and non-covalent interacting forces; van der Waals, hydrogen bonding, π-π and electrostatic interactions [40]. The dominating attractive forces lead to particle aggregation. Providing the necessary repulsive force (electrostatic) hinders the aggregation and self-assemble particles at a finite separation. In the current study, both CNC and GO are negatively charged providing a sufficient counter balance to the attractive force, which brings the rods or sheets to a specific interparticle distance [41]. However, the characteristic of nematic assembly of both CNC and GO self-assemble the rod and sheets in a particular direction. These findings provide the opportunity of using CNC as a spacer between GO sheets to hinder the π-π stacking of the graphene sheets during the reduction process of GO [42]. The controlled self-assembly of nanocellulose/GO suspensions or the reduced nanocellulose-graphene composite allows producing light weight flexible electronics [43], super capacitor [44] and EMI shielding materials [45].

5. Conclusion

The self-assembly mechanism of negatively charged cellulose nanocrystal (CNC) and graphene oxide (GO) aqueous suspensions is studied by SAXS at different CNC/GO concentrations and ratios ranging between 2 and 50 in a suspension. Individually, both GO sheets and CNC rods at low concentration are randomly oriented with a large inter sheet or rod distance as measured by isotropic SAXS scattering. However, once a threshold concentration has been reached, increasing concentration reveals that the GO sheets (or CNC rods) come closer to each other with a decrease in interparticle distance measured. However, after a threshold concentration, the inter sheet or rod repulsion allows the CNC or GO nanoparticles to arrange into the nematic structures. The CNC was mixed with the nematic GO at different weight ratios ranging from 2 to 50. At the lower CNC/GO ratio of 2, the CNC rods disrupt the nematic assembly of the GO suspension. The CNC rods are partially aligned between the GO sheets and the inter rod distance increases to 51 nm. However, increasing further the CNC/GO ratio from 2 to 15 decreases the inter distance to 51 to 42 nm. The higher amount of CNC rods aligns the GO sheets in a partially oriented state. At the CNC/GO ratio 16, there is a sharp decrease in the -inter-rod distance to 38 nm, which is the beginning threshold of the nematic phase. Further increase in ratio from 16 to 50 leads to a linear decrease in the interrod distance to 32 nm. The anisotropic SAXS images reveal the transition from a random distribution to a nematic arrangement. The results disclose that at the lower CNC/GO ratio, multiple GO sheets are intercalated between the CNC rods. Increasing the CNC amount aligns the GO sheets along the direction of the CNC rods assembly. This knowledge gained provides a new perspective in engineering CNC/GO hybrids into advanced technologies for sensors, bio-diagnostics and electronics applications.

CRediT authorship contribution statement

Vikram Singh Raghuwanshi: Writing – original draft, Formal analysis. **Swambabu Varanasi:** Writing – original draft, Formal analysis. **Warren Batchelor:** Formal analysis, Supervision. **Gil Garnier:** Supervision, Writing – original draft.

Declaration of Competing Interest

The authors declare that they have no known competing financial interests or personal relationships that could have appeared to influence the work reported in this paper.

Acknowledgements

Financial support is from Australian Research Council (ARC), Australian Paper, Norske Skog, Orora, and Visy through the Industry Transformation Research Hub grant IH130100016. The authors thank Dr. Md. Joynul Abedin and Prof. Mainak Majumder, Monash University for providing graphene oxide; Ragesh Prathapan for the AFM measurement; Dr. Nigel Kirby beamline scientist of SAXS/WAXS beamline at the Australian Synchrotron for assistance during measurement. Many thanks to the Australian Nuclear Science and Technology Organisation (ANSTO) for providing beamtime.

Appendix A. Supplementary material

Supplementary data to this article can be found online at https://doi.org/10.1016/j.matdes.2022.110572.

References

[1] M.J. Allen, V.C. Tung, R.B. Kaner, Honeycomb Carbon: A Review of Graphene, Chem. Rev. 110 (1) (2010) 132–145.
[2] H.C. Lee, W.W. Liu, S.P. Chai, A.R. Mohamed, A. Aziz, C.S. Khe, N.M.S. Hidayah, U. Hashim, Review of the synthesis, transfer, characterization and growth

mechanisms of single and multilayer graphene, RSC Adv. 7 (26) (2017) 15644–15693.
[3] Y. Li, H. Zhu, S. Zhu, J. Wan, Z. Liu, O. Vaaland, S. Lacey, Z. Fang, H. Dai, T. Li, L. Hu, Hybridizing wood cellulose and graphene oxide toward high-performance fibers, NPG Asia Mater. 7 (1) (2015) e150.
[4] A. Kafy, K.K. Sadasivuni, A. Akther, S.-K. Min, J. Kim, Cellulose/graphene nanocomposite as multifunctional electronic and solvent sensor material, Mater. Lett. 159 (2015) 20–23.
[5] M. Liu, X. Yin, E. Ulin-Avila, B. Geng, T. Zentgraf, L. Ju, F. Wang, X. Zhang, A graphene-based broadband optical modulator, Nature 474 (7349) (2011) 64–67.
[6] D. Shahdeo, A. Roberts, N. Abbineni, S. Gandhi, Chapter Eight - Graphene based sensors, in: C.M. Hussain (Ed.), Comprehensive Analytical Chemistry, Elsevier, 2020, pp. 175–199.
[7] M.S.A. Bhuyan, M.N. Uddin, M.M. Islam, F.A. Bipasha, S.S. Hossain, Synthesis of graphene, International, Nano Lett. 6 (2) (2016) 65–83.
[8] E.M. Pérez, N. Martín, π–π interactions in carbon nanostructures, Chem. Soc. Rev. 44 (18) (2015) 6425–6433.
[9] Z. Li, J. Chu, C. Yang, S. Hao, M.A. Bissett, I.A. Kinloch, R.J. Young, Effect of functional groups on the agglomeration of graphene in nanocomposites, Compos. Sci. Technol. 163 (2018) 116–122.
[10] K. Zhang, L. Ketterle, T. Järvinen, G.S. Lorite, S. Hong, H. Liimatainen, Self-assembly of graphene oxide and cellulose nanocrystals into continuous filament via interfacial nanoparticle complexation, Mater Design 193 (2020) 108791.
[11] G. Huang, C. Hou, Y. Shao, H. Wang, Q. Zhang, Y. Li, M. Zhu, Highly Strong and Elastic Graphene Fibres Prepared from Universal Graphene Oxide Precursors, Sci. Rep.-Uk 4 (1) (2014) 4248.
[12] S. Seiler, C.E. Halbig, F. Grote, P. Rietsch, F. Börrnert, U. Kaiser, B. Meyer, S. Eigler, Effect of friction on oxidative graphite intercalation and high-quality graphene formation, Nat. Commun. 9 (1) (2018) 836.
[13] Y. Zhang, J. Peng, M. Li, E. Saiz, S.E. Wolf, Q. Cheng, Bioinspired Supertough Graphene Fiber through Sequential Interfacial Interactions, ACS Nano 12 (9) (2018) 8901–8908.
[14] S.R. Shin, C. Zihlmann, M. Akbari, P. Assawes, L. Cheung, K. Zhang, V. Manoharan, Y.S. Zhang, M. Yüksekkaya, K.-T. Wan, M. Nikkhah, M.R. Dokmeci, X.(. Tang, A. Khademhosseini, Reduced Graphene Oxide-GelMA Hybrid Hydrogels as Scaffolds for Cardiac Tissue Engineering, Small 12 (27) (2016) 3677–3689.
[15] K.W. Putz, O.C. Compton, C. Segar, Z. An, S.T. Nguyen, L.C. Brinson, Evolution of Order During Vacuum-Assisted Self-Assembly of Graphene Oxide Paper and Associated Polymer Nanocomposites, ACS Nano 5 (8) (2011) 6601–6609.
[16] R. Rao, C.L. Pint, A.E. Islam, R.S. Weatherup, S. Hofmann, E.R. Meshot, F. Wu, C. Zhou, N. Dee, P.B. Amama, J. Carpena-Nuñez, W. Shi, D.L. Plata, E.S. Penev, B.I. Yakobson, P.B. Balbuena, C. Bichara, D.N. Futaba, S. Noda, H. Shin, K.S. Kim, B. Simard, F. Mirri, M. Pasquali, F. Fornasiero, E.I. Kauppinen, M. Arnold, B.A. Cola, P. Nikolaev, S. Arepalli, H.-M. Cheng, D.N. Zakharov, E.A. Stach, J. Zhang, F. Wei, M. Terrones, D.B. Geohegan, B. Maruyama, S. Maruyama, Y. Li, W.W. Adams, A. J. Hart, Carbon Nanotubes and Related Nanomaterials: Critical Advances and Challenges for Synthesis toward Mainstream Commercial Applications, ACS Nano 12 (12) (2018) 11756–11784.
[17] X. Chen, M. Qiu, H. Ding, K. Fu, Y. Fan, A reduced graphene oxide nanofiltration membrane intercalated by well-dispersed carbon nanotubes for drinking water purification, Nanoscale 8 (10) (2016) 5696–5705.
[18] L. Huang, Z. Li, Y. Luo, N. Zhang, W. Qi, E. Jiang, J. Bao, X. Zhang, W. Zheng, B. An, G. He, Low-pressure loose GO composite membrane intercalated by CNT for effective dye/salt separation, Sep. Purif. Technol. 256 (2021) 117839.
[19] C. Zhu, S. Monti, A.P. Mathew, Cellulose Nanofiber-Graphene Oxide Biohybrids: Disclosing the Self-Assembly and Copper-Ion Adsorption Using Advanced Microscopy and ReaxFF Simulations, ACS Nano 12 (7) (2018) 7028–7038.
[20] K.K. Sadasivuni, A. Kafy, L. Zhai, H.-U. Ko, S. Mun, J. Kim, Transparent and Flexible Cellulose Nanocrystal/Reduced Graphene Oxide Film for Proximity Sensing, Small 11 (8) (2015) 994–1002.
[21] F. Wang, L.T. Drzal, Y. Qin, Z. Huang, Multifunctional graphene nanoplatelets/cellulose nanocrystals composite paper, Compos. B Eng. 79 (2015) 521–529.
[22] Y. Lyu, Q.Q. Zhang, Z.X. Wang, J.W. Pu, A Graphene Oxide Nanofiltration Membrane Intercalated with Cellulose Nano-crystals, Bioresources 13 (4) (2018) 9116–9131.
[23] Y. Li, H. Zhu, F. Shen, J. Wan, X. Han, J. Dai, H. Dai, L. Hu, Highly Conductive Microfiber of Graphene Oxide Templated Carbonization of Nanofibrillated Cellulose, Adv. Funct. Mater. 24 (46) (2014) 7366–7372.
[24] P. Liu, C. Zhu, A.P. Mathew, Mechanically robust high flux graphene oxide - nanocellulose membranes for dye removal from water, J. Hazard. Mater. 371 (2019) 484–493.
[25] C. Yan, J. Wang, W. Kang, M. Cui, X.u. Wang, C.Y. Foo, K.J. Chee, P.S. Lee, Highly Stretchable Piezoresistive Graphene-Nanocellulose Nanopaper for Strain Sensors, Adv. Mater. 26 (13) (2014) 2022–2027.
[26] J. Lv, G. Zhang, H. Zhang, F. Yang, Graphene oxide-cellulose nanocrystal (GO-CNC) composite functionalized PVDF membrane with improved antifouling performance in MBR: Behavior and mechanism, Chem. Eng. J. 352 (2018) 765–773.
[27] M.J. Abedin, T.D. Gamot, S.T. Martin, M. Ali, K.I. Hassan, M.S. Mirshekarloo, R.F. Tabor, M.J. Green, M. Majumder, Graphene Oxide Liquid Crystal Domains: Quantification and Role in Tailoring Viscoelastic Behavior, ACS Nano 13 (8) (2019) 8957–8969.
[28] N.M. Kirby, S.T. Mudie, A.M. Hawley, D.J. Cookson, H.D.T. Mertens, N. Cowieson, V. Samardzic-Boban, A low-background-intensity focusing small-angle X-ray scattering undulator beamline, J. Appl. Crystallogr. 46 (6) (2013) 1670–1680.
[29] O. Glatter, O. Kratky, Small-angle X-ray Scattering, Academic Press, London, 1982.
[30] J. Georgieva, E. Valova, I. Mintsouli, S. Sotiropoulos, D. Tatchev, S. Armyanov, A. Hubin, J. Dille, A. Hoell, V. Raghuwanshi, N. Karanasios, L. Malet, Pt(Ni) electrocatalysts for methanol oxidation prepared by galvanic replacement on TiO_2 and TiO_2–C powder supports, J. Electroanal. Chem. 754 (2015) 65–74.
[31] V.S. Raghuwanshi, U.M. Garusinghe, P. Raj, N. Kirby, A. Hoell, W. Batchelor, G. Garnier, Cationic polyacrylamide induced nanoparticles assembly in a cellulose nanofiber network, J. Colloid Interface Sci. 529 (2018) 180–186.
[32] V.S. Raghuwanshi, M. Ochmann, A. Hoell, F. Polzer, K. Rademann, Deep Eutectic Solvents for the Self-Assembly of Gold Nanoparticles: A SAXS, UV–Vis, and TEM Investigation, Langmuir 30 (21) (2014) 6038–6046.
[33] Y.H. Shim, K.E. Lee, T.J. Shin, S.O. Kim, S.Y. Kim, Wide concentration liquid crystallinity of graphene oxide aqueous suspensions with interacting polymers, Mater. Horiz. 4 (6) (2017) 1157–1164.
[34] D.J. Sprouster, C. Sun, Y. Zhang, S.N. Chodankar, J. Gan, L.E. Ecker, Irradiation-Dependent Helium Gas Bubble Superlattice in Tungsten, Sci. Rep. 9 (1) (2019) 2277.
[35] V.S. Raghuwanshi, M. Ochmann, F. Polzer, A. Hoell, K. Rademann, Self-assembly of gold nanoparticles on deep eutectic solvent (DES) surfaces, Chem. Commun. 50 (63) (2014) 8693–8696.
[36] J. Van Rie, G. González-Rubio, S. Kumar, C. Schütz, J. Kohlbrecher, M. Vanroelen, T. Van Gerven, O. Deschaume, C. Bartic, L.M. Liz-Marzán, G. Salazar-Alvarez, W. Thielemans, SANS study of mixed cholesteric cellulose nanocrystal – gold nanorod suspensions, Chem. Commun. 56 (85) (2020) 13001–13004.
[37] C. Schütz, M. Agthe, A.B. Fall, K. Gordeyeva, V. Guccini, M. Salajková, T.S. Plivelic, J.P.F. Lagerwall, G. Salazar-Alvarez, L. Bergström, Rod Packing in Chiral Nematic Cellulose Nanocrystal Dispersions Studied by Small-Angle X-ray Scattering and Laser Diffraction, Langmuir 31 (23) (2015) 6507–6513.
[38] M. Lin, V.S. Raghuwanshi, C. Browne, G.P. Simon, G. Garnier, Modulating transparency and colour of cellulose nanocrystal composite films by varying polymer molecular weight, J. Colloid Interf. Sci. 584 (2021) 216–224.
[39] K. Yao, Q. Meng, V. Bulone, Q. Zhou, Flexible and Responsive Chiral Nematic Cellulose Nanocrystal/Poly(ethylene glycol) Composite Films with Uniform and Tunable Structural Color, Adv. Mater. 29 (28) (2017) 1701323.
[40] Y.J. Min, M. Akbulut, K. Kristiansen, Y. Golan, J. Israelachvili, The role of interparticle and external forces in nanoparticle assembly, Nat. Mater. 7 (7) (2008) 527–538.
[41] C. Bruel, T.S. Davies, P.J. Carreau, J.R. Tavares, M.C. Heuzey, Self-assembly behaviors of colloidal cellulose nanocrystals: A tale of stabilization mechanisms, J. Colloid Interf. Sci. 574 (2020) 399–409.
[42] G.Y. Chen, T. Chen, K. Hou, W.J. Ma, M. Tebyetekerwa, Y.H. Cheng, W. Weng, M. F. Zhu, Robust, hydrophilic graphene/cellulose nanocrystal fiber-based electrode with high capacitive performance and conductivity, Carbon 127 (2018) 218–227.
[43] A. Ahmed, B. Adak, M.O. Faruk, S. Mukhopadhyay, Nanocellulose Coupled 2D Graphene Nanostructures: Emerging Paradigm for Sustainable Functional Applications, Ind. Eng. Chem. Res. 60 (30) (2021) 10882–10916.
[44] A. Brakat, H. Zhu, Nanocellulose-Graphene Derivative Hybrids: Advanced Structure-Based Functionality from Top-down Synthesis to Bottom-up Assembly, ACS App. Bio Mater. 4 (10) (2021) 7366–7401.
[45] W.X. Yang, Y. Zhang, T.Y. Liu, R. Huang, S.G. Chai, F. Chen, Q. Fu, Completely Green Approach for the Preparation of Strong and Highly Conductive Graphene Composite Film by Using Nanocellulose as Dispersing Agent and Mechanical Compression, Acs Sustain. Chem. Eng. 5 (10) (2017) 9102–9113.
[46] M. Girard, D. Vidal, F. Bertand, J.R. Tavares, M. Heuzey, Evidence-based guidelines for the ultrasonic dispersion of cellulose nanocrystals, Ultrason. Sonochem. 71 (2021) 105378.
[47] H. Cho, A. Shakil, A.A. Polycarpou, S. Kim, Enabling Selectively Tunable Mechanical Properties of Graphene Oxide/Silk Fibroin/Cellulose Nanocrystal Bionanofilms, ACS Nano 15 (2021) 19546–19558.